Supplemental Material

Supplementary Materials for

The impacts of adjusting momentum roughness length on strong and weak hurricanes forecasts: a comprehensive analysis of weather simulations and observations

Meng Li[1], Jun A. Zhang[2,3], Leo Matak[1], and Mostafa Momen[1,*]

[1]*Department of Civil and Environmental Engineering, University of Houston, Houston, Texas, USA*

[2] *NOAA/AOML/Hurricane Research Division, Miami, Florida, USA*

[3]*Cooperative Institute for Marine and Atmospheric Studies, Miami, Florida*

**Corresponding author*: Dr. Mostafa Momen, Email: mmomen@uh.edu

Contents of this file

Supplementary Texts S1-S6, Supplementary Figures S1 to S10, Supplementary References

Table of Contents

S1. Details of the governing equations for the atmospheric and wave models

The atmospheric model

We employ the Advanced Research WRF (ARW) core of version 4.2.2 WRF modeling system to simulate hurricanes. The WRF model is an extensively used atmospheric modeling system designed for numerical weather prediction (Skamarock et al. 2008). The ARW solver of the WRF model features the fully compressible non-hydrostatic Eulerian equations with available hydrostatic options. It adopts the Arakawa C-grid in the horizontal directions, e.g., the east-west velocity component. In the vertical direction, a terrain-following sigma coordinate based on the hydrostatic pressure (Park et al. 2013; Laprise 1992) is employed. The governing equations continuity and momentum equations of WRF can be written as

$\partial_t \mu_d + \partial_j U_j = 0$,

$\partial_t U_i + u_i \partial_j U_j + \mu_d \alpha \partial_i p + \frac{\alpha}{\alpha_d} \partial_\eta p \partial_i \varphi (\delta_{i1} + \delta_{i2}) - g \left(\frac{\alpha}{\alpha_d} \partial_\eta p - \mu_d \right) \delta_{i3} = F_i.$

η denotes the vertical coordinate as $\eta = \frac{p_d - p_t}{p_s - p_t}$, where p_d is the hydrostatic pressure, p_s and p_t are respectively the hydrostatic pressure at the bottom and top boundaries. In the above equations, $u_i = (u, v, w)$ for $i = (x, y, \eta)$ is the covariant velocity in horizontal and vertical directions. The vertical coordinate metric is defined as $\mu_d = \frac{\partial p_d}{\partial \eta}$ and $U_i = \mu_d u_i$ is the velocity in flux form. The inverse density of dry air and the inverse density of the full parcel of air are defined as α_d and α. g is the gravitational acceleration and φ is the geopotential height. Here, the full pressure p is the sum of the water vapor and dry air pressures. The right-hand side F_i is the forcing term that represents the model physics, projections, sinks, and sources.

Instead of resolving the eddy down to their smallest scales, the Planetary Boundary Layer (PBL) scheme is used to model the sub grid scale (SGS) fluxes in the entire atmospheric column including the mixed boundary layer and the stable layer. Previous studies show that there are significant differences between the hurricane boundary layer and the regular atmospheric boundary layer (Momen et al. 2021; Zhang et al. 2017, 2009, 2011; Zhang 2010; Li et al. 2019). In the current study, the Yonsei University scheme (YSU) PBL scheme (Hong et al. 2006; Hong 2010) and Mellor-Yamada-Janjic (MYJ) PBL scheme are considered (Janjić 1990, 1994; Mellor and Yamada 1982).

For all simulated cases, the initial and boundary conditions are obtained from the National Centers for Environmental Prediction (NCEP) FNL Operational Global Analysis data (NCEP National Centers for Environmental Prediction/National Weather Service/NOAA/US Department of Commerce 2000). This data is from the Global Data Assimilation System (GDAS) and the FNLs are made in the Global Forecast System (GFS). The initial and boundary conditions are available on 1-degree resolution and provided operationally every six hours. For the atmospheric simulations, the time steps are selected to ensure the Courant-Friedrichs-Lewy (CFL) values based on the maximum wind speed to not exceed 0.5.

The wave model

The wave model adopted in this study is Simulating Waves Nearshores (SWAN). SWAN is a third-generation wave model mainly used for simulating wind-generated surface gravity waves by solving the Eulerian formulation of the two-dimensional discrete spectral balance of action density equation with many different types of parameterizations including wind wave growth, white capping, wave breaking, and wave-wave interaction (Ris et al. 1999). The evolution of the wave spectrum can be described as follows (Holthuijsen 2010; Hasselmann et al. 1973)

$$\frac{\partial N}{\partial t}+\frac{\partial c_x N}{\partial x}+\frac{\partial c_y N}{\partial y}+\frac{\partial c_\sigma N}{\partial \sigma}+\frac{\partial c_\theta N}{\partial \theta}=\frac{S}{\sigma},$$

where $N(x,y,\sigma,\theta)=E(x,y,\sigma,\theta)/\sigma$ is the action density spectrum, and $E(x,y,\sigma,\theta)$ shows the wave energy density spectrum. In this formula, x and y are Cartesian coordinates, σ is the relative frequency as observed in a frame of reference moving with the current, and θ is the wave direction normal to the wave crest of each spectral component. The first term on the left-hand side denotes the local change rate of action density in time, the second and third terms represent the propagation of wave action density in geographic space with wave group velocities c_x and c_y, respectively. The fourth term is the changes of the relative frequency due to the velocity c_σ in the frequency space, and the fifth term is the refraction due to the c_θ in the directional space.

Previous studies have shown that the action density spectrum $N(x,y,\sigma,\theta)$ is conserved in the presence of the ambient ocean current while the energy density spectrum is not (Warner et al. 2010; Ris et al. 1999). If the wave spectrum is represented by the action density spectrum $N(x,y,\sigma,\theta)$, the balance equation would be a hyperbolic type of equation. One of the features of the hyperbolic equation is that it retains the initial disturbances. The state in a grid point is

determined directly by that in the upwave grid point. Thus, a first-order implicit upwind scheme is formulated to discretize the SWAN governing equation in both the geographical and spectral space. For the spectral space, a second-order central approximation is supplemented.

The Coupled Ocean-Atmosphere-Wave-Sediment Transport (COAWST) Modeling System (Zambon et al. 2014; Olabarrieta et al. 2012; Warner et al. 2010) is used for the WRF-SWAN coupled cases in this study. The Model Coupling Toolkit (MCT) is selected as the coupler in the COAWST system to exchange data fields between the atmospheric model, the ocean model, the wave model, and the Community Sediment Transport Model (Jacob et al. 2005; Warner et al. 2008). In this paper, the atmospheric model WRF-ARW provides surface wind speed at 10m – U_{10} and V_{10} – to the wave model SWAN. Then, the wave model SWAN estimates the significant wave height H_w and mean wavelength L_w for calculating the aerodynamic roughness length in the WRF-ARW atmospheric model. The two-way coupled system is made possible by the MCT coupler.

For the wave simulations, SWAN has four options for the initial condition. The default initial spectra are computed from local wind velocities with a Joint North Sea Wave Project (JONSWAP) shape. The second option is the zero initial spectral densities, meaning that the waves are generated in the wave model only by the wind. The third option is to set the wave spectrum in the entire computational domain based on wave parameters like significant wave height, peak or mean wave period, etc. The fourth option is to read the initial wave field from restart files. In this study, after testing all the options, we select the third option to create a JONSWAP wave spectrum. For strong hurricanes, the significant wave height is set to 8 m and the mean wave period is set to 14 s. For weak hurricanes, the significant wave height and the mean wave period are 4 m and 7 s, respectively. This setting provided the best results for the considered hurricane cases. In the directional space, the number of mesh is set to 36, while in the frequency space, the number of mesh is set to 25 with the frequency ranges from the 0.04 Hz to 1 Hz.

S2. The sensitivity of category 3-5 hurricane forecasting accuracy to various models and values of surface momentum roughness length

We also examined the sensitivity of surface momentum roughness to category 3-5 hurricane forecasting accuracy using different models including WRF-COAWST, WRF-YSU-1, and WRF-

YSU-2. The hurricane intensity, track, and surface roughness are depicted in Figs. S1, S2, and S3, respectively. As indicated in the results, the overall intensity predictions in these strong hurricanes are improved among the three considered models using the relatively smaller surface momentum roughness length values.

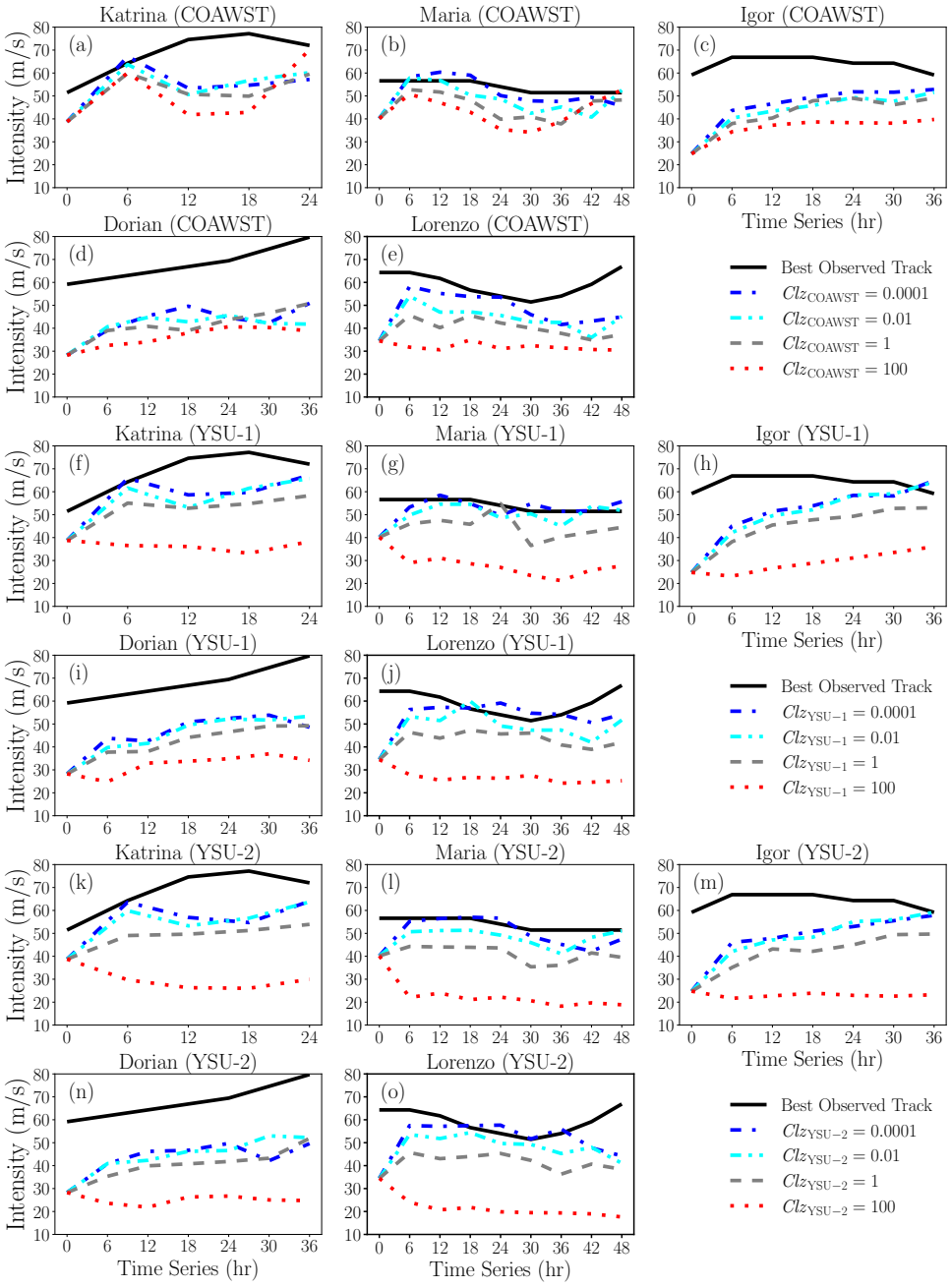

FIG. S1 | The hurricane intensity with various surface momentum roughness lengths from different models using 8 km grid spacings.

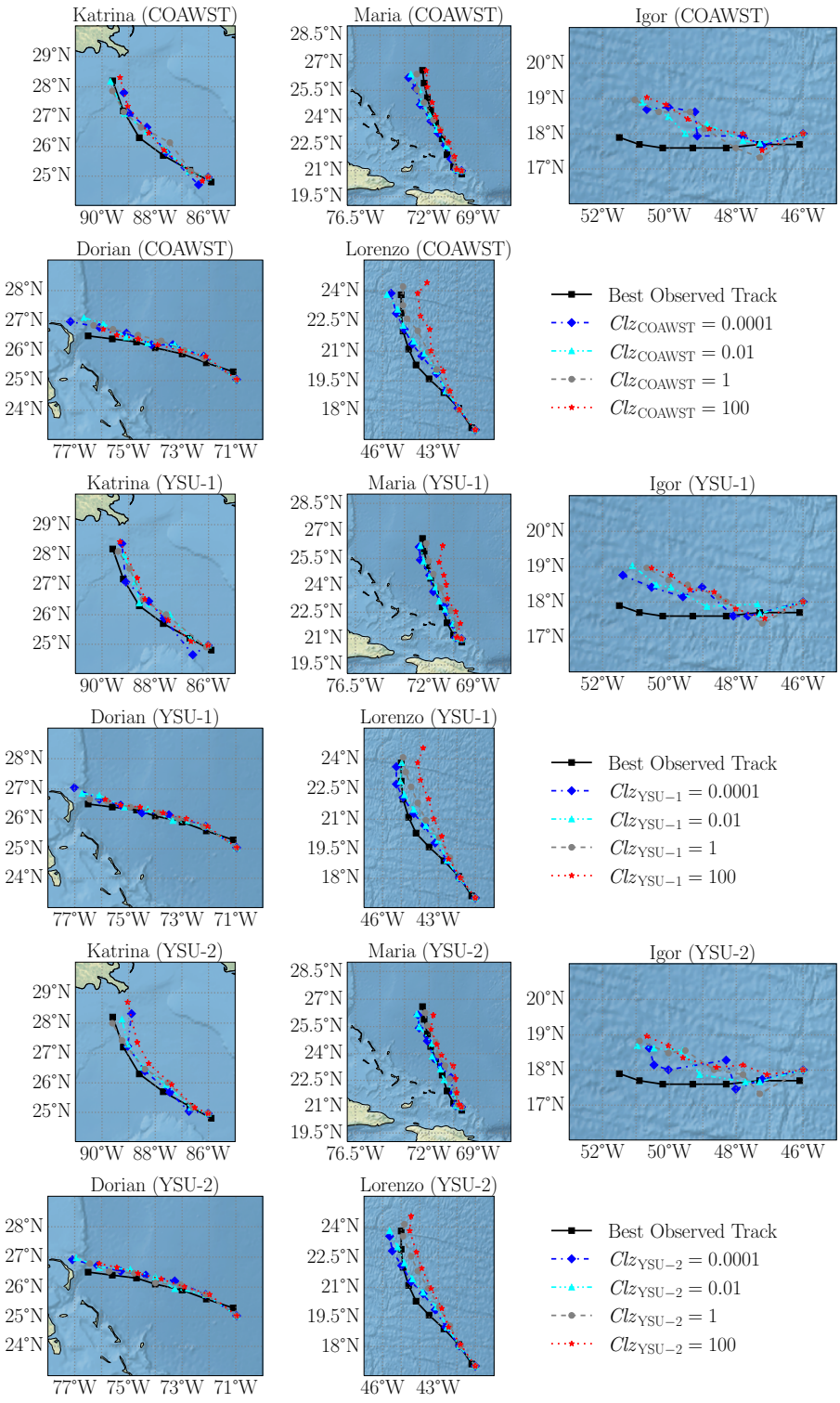

FIG. S2 | The hurricane track with various surface momentum roughness lengths from different models using 8 km grid spacings.

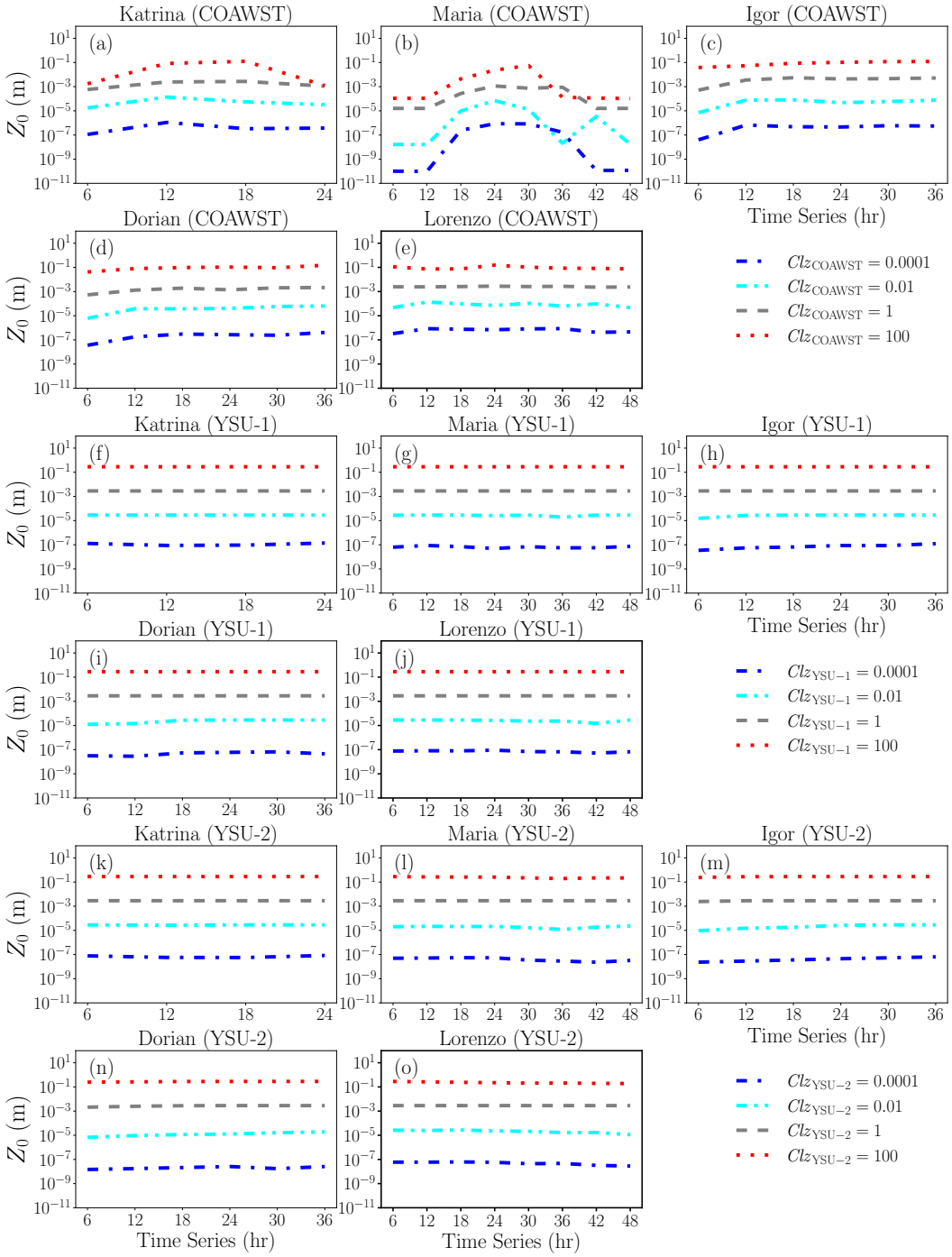

FIG. S3 | The averaged surface momentum roughness over the hurricane eyewalls with various surface momentum roughness lengths from different models using 8 km grid spacings.

S3. The sensitivity of category 1-2 hurricane forecasting accuracy to various models and values of surface momentum roughness length

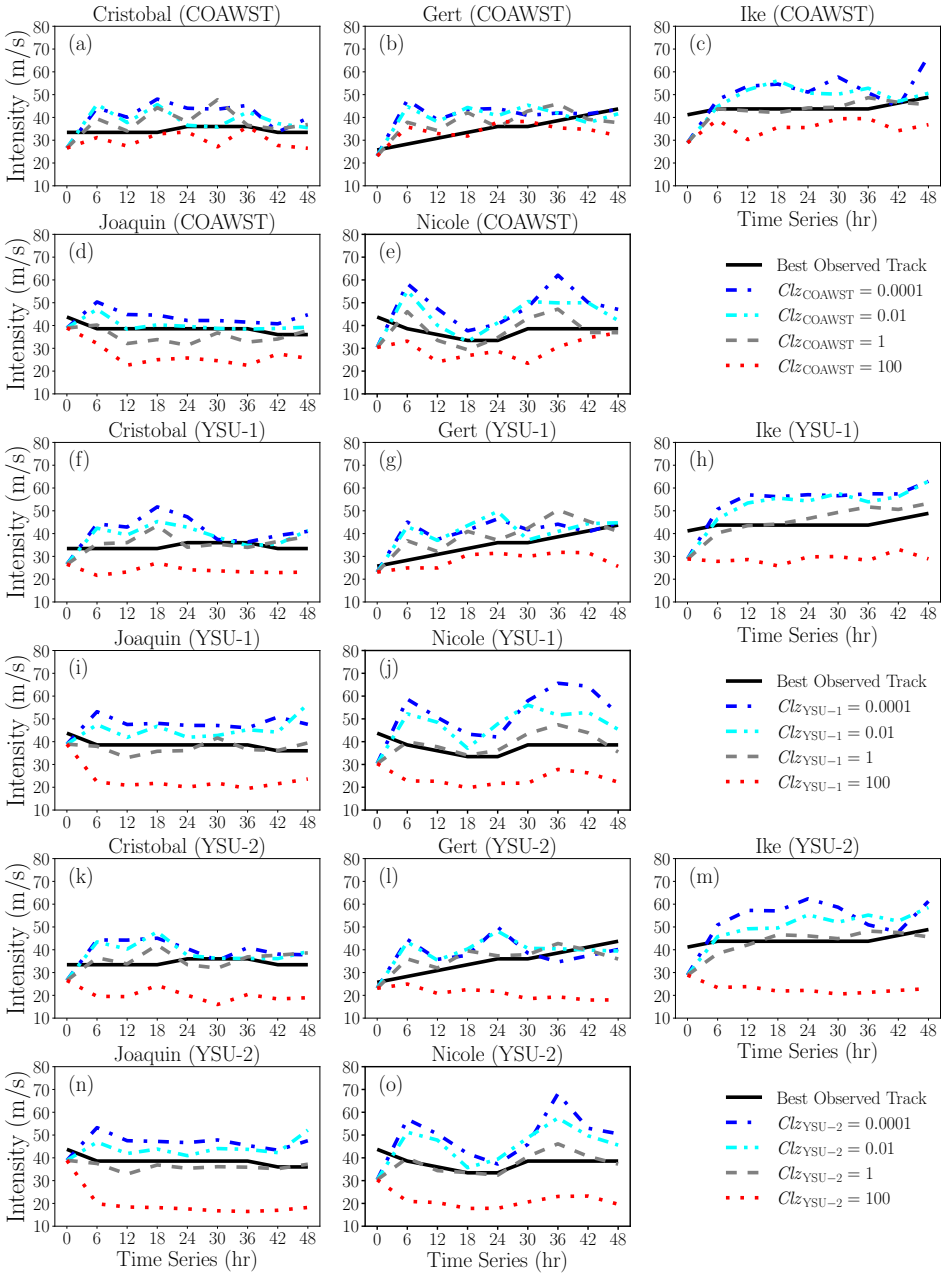

FIG. S4 | Weak hurricanes intensity timeseries for various surface momentum roughness length models using 8 km grid spacings.

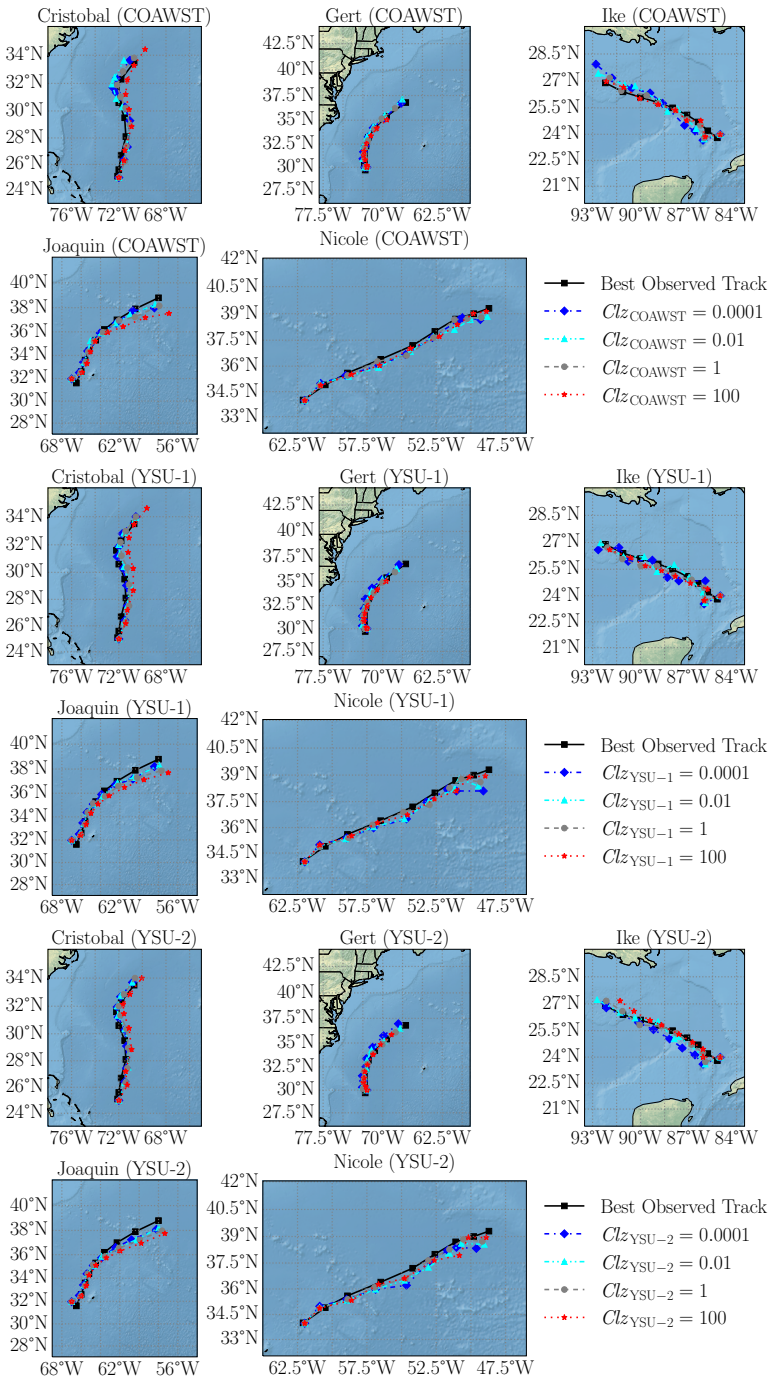

FIG. S5 | Weak hurricanes track with various surface momentum roughness lengths from different models using 8 km grid spacings.

The sensitivity of surface momentum roughness to category 1-2 hurricane forecasting accuracy using different models including WRF-COAWST, WRF-YSU-1, and WRF-YSU-2 are investigated in this section. The hurricane intensity and track are depicted in Figs. S4, and S5,

respectively. Different from the strong hurricanes, for the weak hurricanes, the default cases outperform other cases, indicating that the original surface momentum roughness is optimum for considered category 1-2 hurricanes.

S4. The impacts of surface momentum roughness on hurricane forecasting using various grid spacings

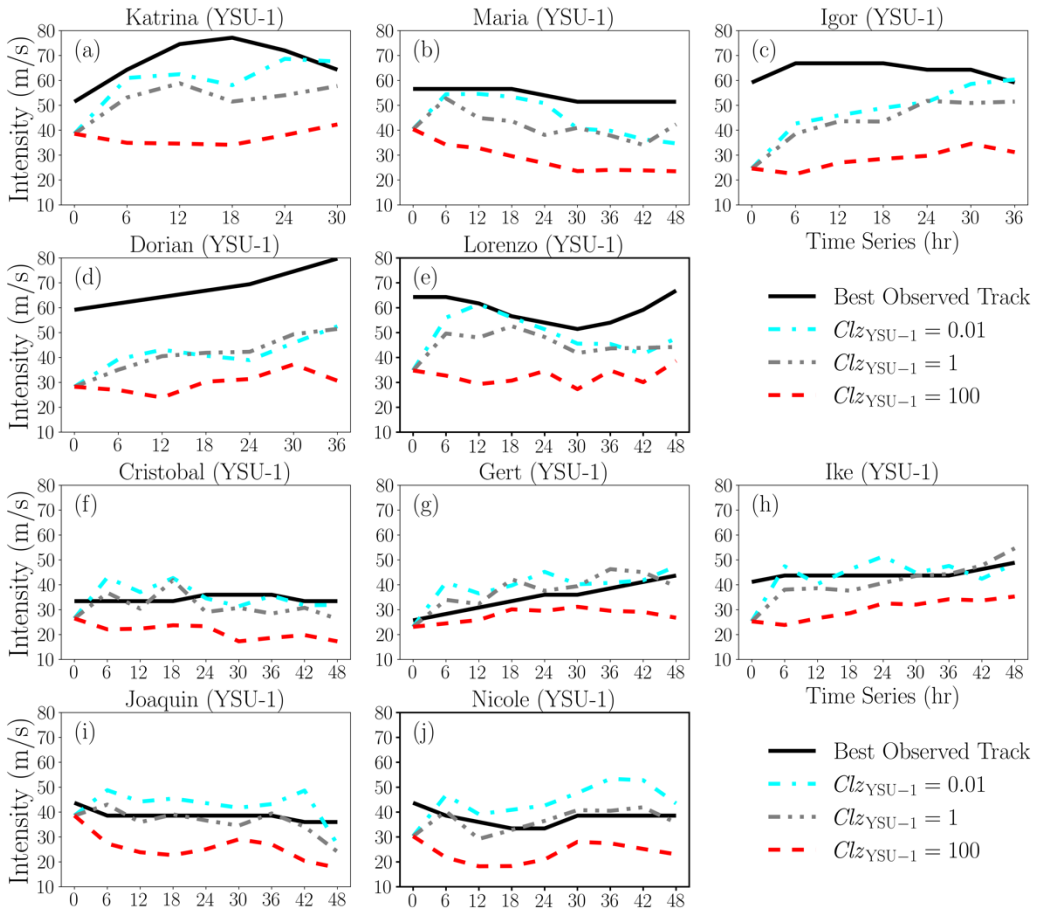

FIG. S6 | The time series of hurricane intensity with various surface momentum roughness lengths for WRF-YSU-1 using 2 km grid spacings.

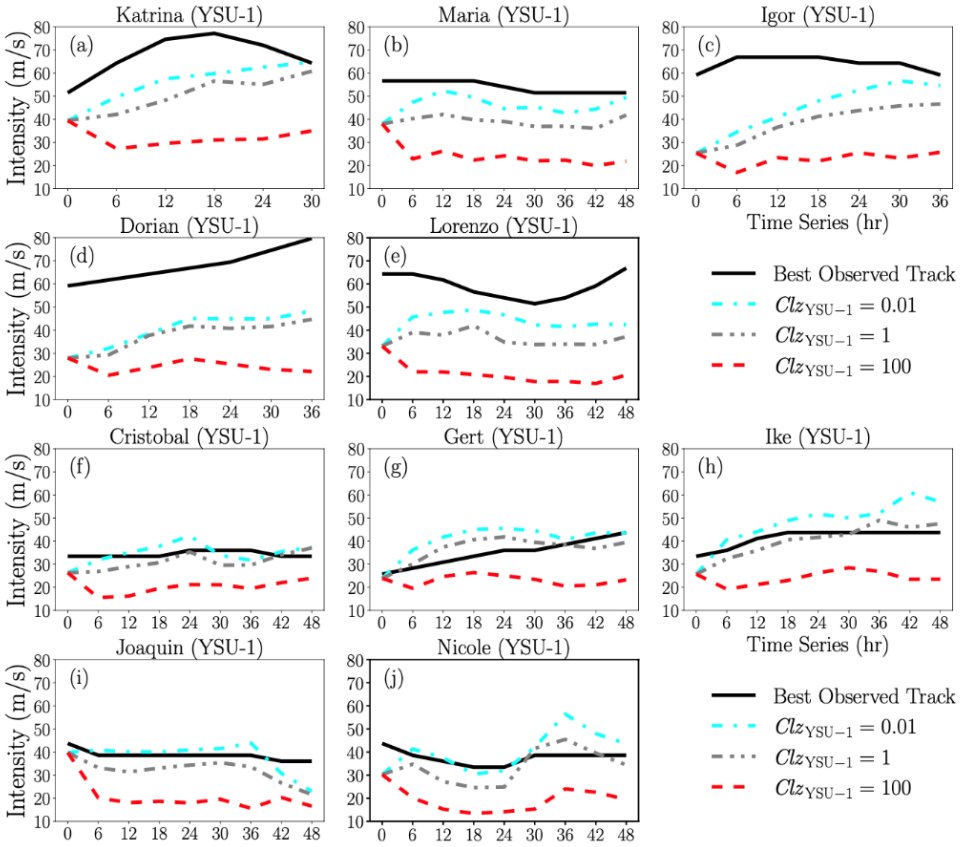

FIG. S7 | The time series of hurricane intensity with various surface momentum roughness lengths for WRF-YSU-1 using 32 km grid spacings.

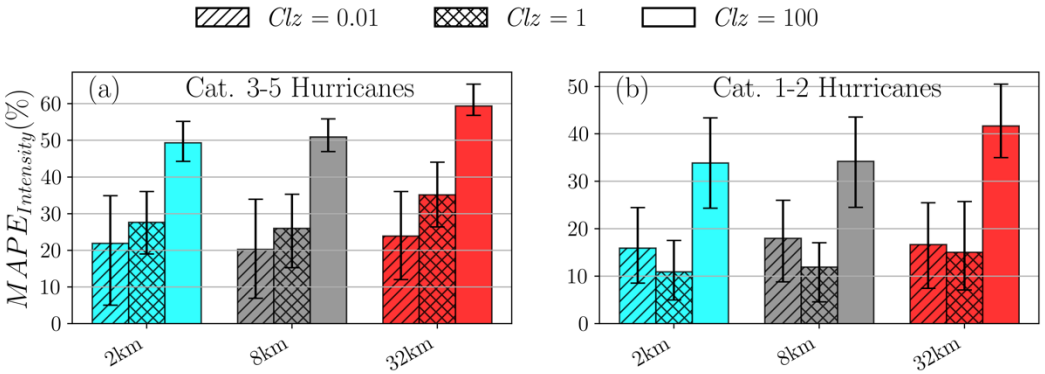

FIG. S8 | The normalized intensity MAPE with various surface momentum roughness lengths for WRF-YSU-1 using 2 km, 8 km and 32 km grid spacings. The error bars show the range from the 20th percentile to the 80th percentile. (a) shows the statistics for category 3-5 hurricanes, while (b) shows the statistics for category 1-2 hurricanes.

To examine the grid resolution dependency of our results, we carried out three computational grid spacings of 2 km, 8 km, and 32 km for WRF-YSU-1. The time series of hurricane intensity for 2km and 32km are show in figure S6 and S7. Figure S8 shows the normalized intensity MAPE. For category 3-5 hurricanes, compared with cases using the default momentum roughness, decreasing the surface roughness length improves the wind intensity regardless of the grid resolution. On the other hand, for category 1-2 hurricanes, the cases using the default momentum roughness perform the best. These results show that our findings on the impacts of surface momentum roughness on hurricane forecasting accuracy are general and applicable for different grid resolution simulations.

S5. Mean Absolute Error Metric

We also calculated the absolute error metric for wind intensity of the default cases. As Fig. S9 indicates, the results are similar to MAPE, and YSU-1 has the best performance in predicting the intensity of the hurricanes in the considered cases.

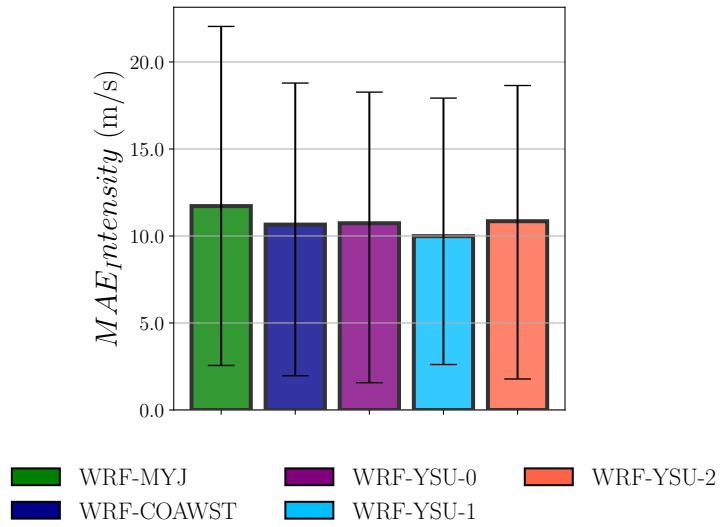

FIG. S9 | Overview of the simulated results for hurricane absolute mean 10 m wind intensity forecast errors from different models using their default momentum roughness lengths with 8 km grid spacing. The error bars show the range from the 20th percentile to the 80th percentile of the errors. In total, 450 samples from 50 simulations (10 hurricanes × 5 models) were used.

S6. Impacts on Wind-Speed Radius Profile

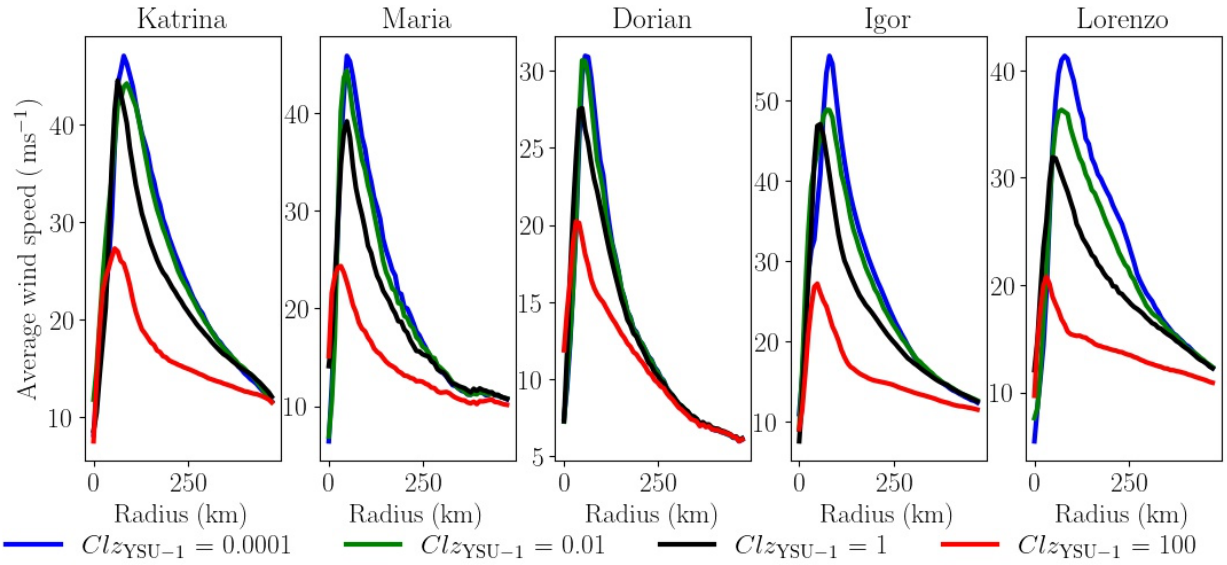

Fig. S10 | 8-km radially averaged wind speed-radius plot for five strong hurricane cases in the first or last 12 h of simulation.

To investigate how the change in surface momentum roughness impacts the wind speed-radius profiles, Fig. S10 shows the radially averaged wind speed-radius plots. As the figure indicates, the maximum surface wind (peak of the profiles in Fig. S10) decreases by increasing z_0. The radius of the maximum wind (RMW) does not appear to change significantly with changing the surface roughness (increasing z_0 seems to weaken the hurricane and make it smaller in general).

S7. The hurricane wind profiles for category 3-5 hurricanes using WRF-YSU-1 with various surface momentum roughness lengths

To investigate the impacts of different z_0 values on hurricane boundary layer winds, the wind profiles at the hurricane eyewalls are depicted in figure S11 for different imposed surface momentum roughness length values. Both the radial velocity u_r and tangential velocity u_θ profiles are shown. We find that, compared with the default cases, the magnitude of u_θ close to the ground (up to ~ 500 m) is relatively smaller for cases with larger surface momentum roughness length, while it is relatively larger for cases with smaller surface momentum roughness lengths.

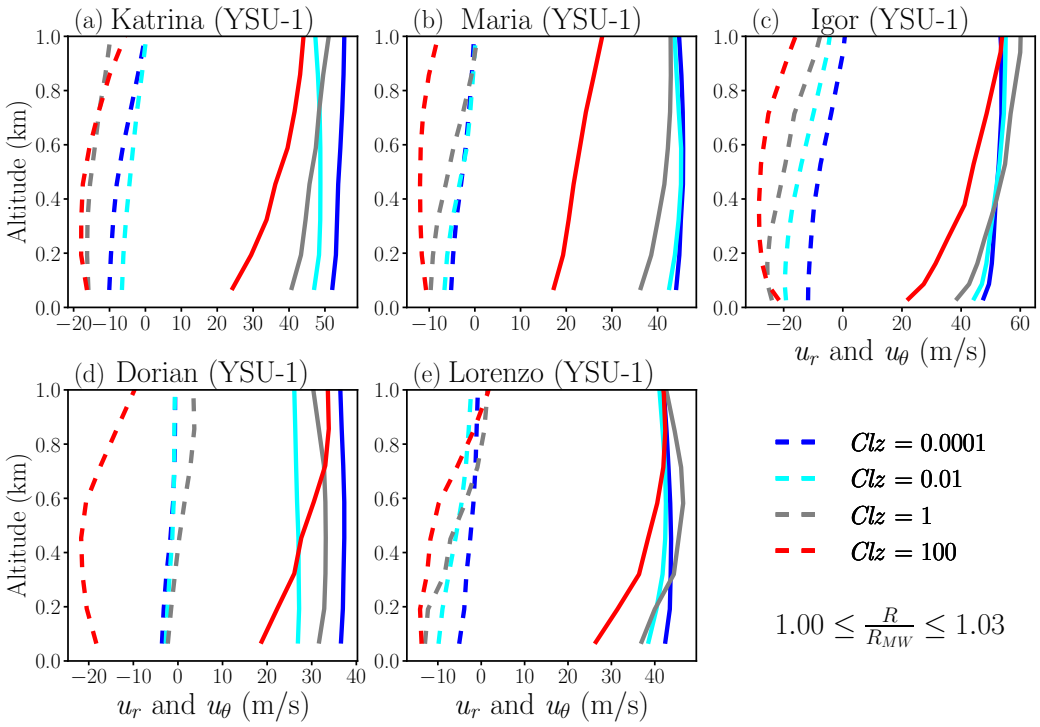

FIG. S11 | The wind profiles at the hurricane eyewalls with various surface momentum roughness lengths from different models using 8 km grid spacings. The dashed lines represent the radial velocity u_r, and the solid lines represent the tangential velocity u_θ. R represents the distance to the hurricane eye, and R_{MW} denotes the radius of the maximum wind speed.

S8. The wind profiles from dropsondes observations

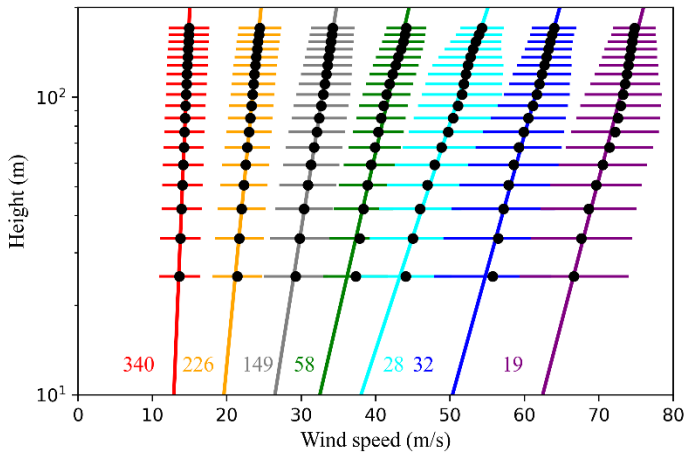

FIG. S12 | The observational data obtained from GPS dropsondes. Different velocity bins are illustrated using different colors. The horizontal line indicates the standard deviation.

TABLE S1 | List of GPS dropsondes count for each hurricane

	Katrina	Maria	Igor	Lorenzo	Joaquin	Ike	Dorian	Cristobal	Sum
Sondes Count	84	28	75	98	118	227	111	111	852

The observational data in figure S12 are taken from 852 high-resolution wind profiles collected with the GPS dropsondes from hurricanes Katrina, Maria, Lorenzo, Igor, Joaquin, Ike, Dorian, and Cristobal (see Table S1 for sondes count). These wind profiles are divided into seven groups based on the 200 m wind speed ranging from 10m/s to 80m/s with a 10 m/s interval. The observed momentum roughness length for each velocity group is obtained by fitting the log law to the mean wind profile and extrapolating it to the zero wind speed similar to previous studies (Holthuijsen et al. 2012; Powell et al. 2003).

REFERENCES

Hasselmann, K. F., and Coauthors, 1973: Measurements of wind-wave growth and swell decay during the Joint North Sea Wave Project (JONSWAP). *Ergaenzungsh. zur Dtsch. Hydrogr. Zeitschrift, R. A*,.

Holthuijsen, L. H., 2010: *Waves in oceanic and coastal waters*. Cambridge university press,.

——, M. D. Powell, and J. D. Pietrzak, 2012: Wind and waves in extreme hurricanes. *J. Geophys. Res. Ocean.*, **117**.

Hong, S., 2010: A new stable boundary-layer mixing scheme and its impact on the simulated East Asian summer monsoon. *Q. J. R. Meteorol. Soc.*, **136**, 1481–1496.

Hong, S. Y., Y. Noh, and J. Dudhia, 2006: A new vertical diffusion package with an explicit treatment of entrainment processes. *Mon. Weather Rev.*, **134**, 2318–2341, https://doi.org/10.1175/MWR3199.1.

Jacob, R., J. Larson, and E. Ong, 2005: M N communication and parallel interpolation in Community Climate System Model Version 3 using the model coupling toolkit. *Int. J. High Perform. Comput. Appl.*, **19**, 293–307.

Janjić, Z. I., 1990: The step-mountain coordinate: Physical package. *Mon. Weather Rev.*, **118**, 1429–1443.

——, 1994: The step-mountain eta coordinate model: Further developments of the convection, viscous sublayer, and turbulence closure schemes. *Mon. Weather Rev.*, **122**, 927–945.

Laprise, R., 1992: The Euler equations of motion with hydrostatic pressure as an independent variable. *Mon. Weather Rev.*, **120**, 197–207.

Li, M., Z. Zhao, Y. Pandya, G. V. Iungo, and D. Yang, 2019: Large-eddy simulations of oil droplet aerosol transport in the marine atmospheric boundary layer. *Atmosphere (Basel).*, **10**, 459.

Mellor, G. L., and T. Yamada, 1982: Development of a turbulence closure model for geophysical fluid problems. *Rev. Geophys.*, **20**, 851–875.

Momen, M., M. B. Parlange, and M. G. Giometto, 2021: Scrambling and reorientation of classical boundary layer turbulence in hurricane winds. *Geophys. Res. Lett.*, **48**, https://doi.org/https://doi.org/10.1029/2020GL091695.

NCEP National Centers for Environmental Prediction/National Weather Service/NOAA/US Department of Commerce, 2000: NCEP FNL operational model global tropospheric analyses, continuing from July 1999. *Res.*

Data Arch. Natl. Cent. Atmos. Res. Comput. Inf. Syst. Lab.,.

Olabarrieta, M., J. C. Warner, B. Armstrong, J. B. Zambon, and R. He, 2012: Ocean–atmosphere dynamics during Hurricane Ida and Nor'Ida: An application of the coupled ocean–atmosphere–wave–sediment transport (COAWST) modeling system. *Ocean Model.*, **43**, 112–137.

Park, S.-H., W. C. Skamarock, J. B. Klemp, L. D. Fowler, and M. G. Duda, 2013: Evaluation of global atmospheric solvers using extensions of the Jablonowski and Williamson baroclinic wave test case. *Mon. Weather Rev.*, **141**, 3116–3129.

Powell, M. D., P. J. Vickery, and T. A. Reinhold, 2003: Reduced drag coefficient for high wind speeds in tropical cyclones. *Nature*, **422**, 279–283, https://doi.org/10.1038/nature01481.

Ris, R. C., L. H. Holthuijsen, and N. Booij, 1999: A third-generation wave model for coastal regions: 2. Verification. *J. Geophys. Res. Ocean.*, **104**, 7667–7681.

Skamarock, W. C., J. B. Klemp, D. O. Gill, D. M. Barker, M. G. Duda, W. Wang, and J. G. Powers, 2008: A Description of the Advanced Research WRF Version 3. *NCAR Tech. NOTE*,.

Warner, J. C., N. Perlin, and E. D. Skyllingstad, 2008: Using the Model Coupling Toolkit to couple earth system models. *Environ. Model. Softw.*, **23**, 1240–1249.

——, B. Armstrong, R. He, and J. B. Zambon, 2010: Development of a coupled ocean–atmosphere–wave–sediment transport (COAWST) modeling system. *Ocean Model.*, **35**, 230–244.

Zambon, J. B., R. He, and J. C. Warner, 2014: Investigation of hurricane Ivan using the coupled ocean–atmosphere–wave–sediment transport (COAWST) model. *Ocean Dyn.*, **64**, 1535–1554.

Zhang, J. A., 2010: Spectral characteristics of turbulence in the hurricane boundary layer over the ocean between the outer rain bands. *Q. J. R. Meteorol. Soc.*, **136**, 918–926, https://doi.org/10.1002/qj.610.

Zhang, J. A., W. M. Drennan, P. G. Black, and J. R. French, 2009: Turbulence Structure of the Hurricane Boundary Layer between the Outer Rainbands. *J. Atmos. Sci.*, **66**, 2455–2467, https://doi.org/10.1175/2009JAS2954.1.

Zhang, J. A., R. F. Rogers, D. S. Nolan, and F. D. Marks, 2011: On the characteristic height scales of the hurricane boundary layer. *Mon. Weather Rev.*, **139**, 2523–2535, https://doi.org/10.1175/MWR-D-10-05017.1.

——, ——, and V. Tallapragada, 2017: Impact of parameterized boundary layer structure on tropical cyclone rapid intensification forecasts in HWRF. *Mon. Weather Rev.*, **145**, 1413–1426, https://doi.org/10.1175/MWR-D-16-0129.1.